Journal of Energy Storage 92 (2024) 112042

Contents lists available at ScienceDirect

Journal of Energy Storage

journal homepage: www.elsevier.com/locate/est

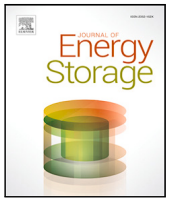

Research papers

Towards robust state estimation for LFP batteries: Model-in-the-loop analysis with hysteresis modelling and perspectives for other chemistries

Dominik Jöst [a,b,f,*,1], Lakshimi Narayanan Palaniswamy [a,c,1], Katharina Lilith Quade [a,b,f], Dirk Uwe Sauer [a,b,d,e,f]

[a] Chair for Electrochemical Energy Conversion and Storage Systems, Institute for Power Electronics and Electrical Drives (ISEA), RWTH Aachen University, Campus-Boulevard 89, 52074 Aachen, Germany
[b] Center for Ageing, Reliability and Lifetime Prediction for Electrochemical and Power Electronic Systems (CARL), RWTH Aachen University, Campus-Boulevard 89, 52074 Aachen, Germany
[c] Battery Technology Center, Institute of Electrical Engineering, Karlsruhe Institute of Technology (KIT), Hermann-von-Helmholtz-Platz 1, 76344 Eggenstein-Leopoldshafen, Germany
[d] Helmholtz Institute Münster: Ionics in Energy Storage (HI MS), IEK 12, Forschungszentrum Jülich, 52425 Jülich, Germany
[e] Institute for Power Generation and Storage Systems (PGS), E.ON Energy Research Center (E.ON ERC), RWTH Aachen University, Mathieustrasse 10, 52074 Aachen, Germany
[f] Jülich Aachen Research Alliance, JARA Energy, Templergraben 55, 52056 Aachen, Germany

ARTICLE INFO

Dataset link: https://doi:10.18154/RWTH-2024-03667

Keywords:
Battery management system
Stationary storage system
Lithium iron phosphate
Hysteresis modelling
Kalman filter
Particle filter

ABSTRACT

The accurate estimation of a battery's state of charge (SOC) is critical in battery management systems for various applications. Lithium Iron Phosphate (LFP) batteries, preferred for their long cycle life, cost efficiency, and enhanced safety, have emerged as favourable choices for stationary storage. Yet, they still face challenges in precise SOC estimation due to the flatness and hysteresis of their open circuit voltage. Addressing this, our study integrates a hysteresis model into a third-order battery model for BMS controlling a stationary storage system in frequency containment reserve (FCR) application. We analysed three advanced SOC estimation techniques — extended Kalman filter (EKF), dual unscented Kalman filter (DUKF), and particle filter (PF) — with the hysteresis model using a model-in-the-loop (MiL) toolchain. Performance testing under a 48-hour FCR load profile showed EKF with a 4% error, DUKF achieving the best result with a 1.1% error, and PF's performance varying between 2.9% and 4% depending on particle count. Robustness tests against initialization and current sensor errors under an 8 hr profile revealed DUKF maintained a 2% error boundary irrespective of the error introduced, highlighting the hysteresis model's effectiveness. Broadening the scope, the study also explores extending the method to other lithium-ion chemistries.

1. Introduction

Currently, the energy sector is witnessing a massive changeover, with multiple policies and initiatives to set pathways to decarbonization [1]. This has led to the massive adoption of power generation from various renewable energy sources (RES) [2]. Electrical energy storage (EES) improves the reliability and overall use of the entire power system and in the form of batteries offers rapid response capabilities while still having reasonable energy density [3]. This makes it a suitable technology for primary control of the electricity grid with services such as frequency control and voltage regulation [4]. Favourably, with the recent increase in Electric Vehicle (EV) sales numbers, prices of lithium-ion batteries (LIBs) have been steadily decreasing [5,6]. Thus, due to economic and technical suitability, the LIB technology is now being considered extensively for stationary storage applications both as large-scale storage systems (LSS) and home storage systems [7,8]. In 2017, across the vast stationary storage installations around the world, electrochemical storage systems accounted for 1.6 GW (2.8 bn€), of which LIB alone accounted for 81% (in terms of power capacity), i.e. 1.3 GW (0.85 bn€) [5]. Additionally, as per the projections of IRENA, this installed stationary storage capacity as of 2017 would increase by 9 to 15-folds in a standard case or 17 to 38-folds in a doubling case by 2030 [9]. Cells with Lithium Iron Phosphate (LFP), Lithium Nickel Cobalt Aluminium Oxide (NCA) or Lithium Nickel Manganese Cobalt Oxide (NMC) cathodes and Graphite or Lithium Titanate Oxide (LTO)

* Corresponding author.
E-mail addresses: batteries@isea.rwth-aachen.de, dominik.joest@isea.rwth-aachen.de (D. Jöst).
[1] These authors contributed equally.

https://doi.org/10.1016/j.est.2024.112042
Received 24 January 2024; Received in revised form 9 April 2024; Accepted 12 May 2024

Nomenclature

$\bar{\mathcal{X}}$	Resampled particles at step k
Δt	Time difference between steps (s)
$\hat{\mathbf{x}}_k^+$, $\hat{\boldsymbol{\theta}}_k^+$	Post priori state at step k
$\hat{\mathbf{x}}_k^-$, $\hat{\boldsymbol{\theta}}_k^-$, $\mathbf{X}_k^*$	Priori state at step k
$\mathbf{X}_k^+$	Sigma points or particles at step k
$\mathbf{Y}_k^*$	Estimated output at step k
Ψ	Factor depicting position of OCV during transition from charging to discharging direction
$\mathbf{q}_k^{[i]}$	Weight/likelihood of particle i at step k
$\mathbf{w}_k^{[i]}$	Normalized weight/likelihood of particle i at step k
θ_k	Battery parameters at step k
A, B	State matrices of the battery model
C_{nom}	Nominal capacity of cell (Ah)
I_{cell}	Current through the cell (A)
k	Time step
M	Number of particles used in particle filter
$m_{\text{i}}, m_{\text{ii}}$	Hysteresis coefficients of ith integral
N	Number of sigma points
n	Count of integrals representing hysteresis
u_k	Inputs to state space at step k
U_{cell}	Cell terminal voltage (V)
v_k	Measurement noise at step k
w_k	System noise at step k
x_k	State at step k
y_k	Output of stat space representation at step k

anodes are the common options for lithium-ion battery applications. LFP, in particular, distinguishes itself due to its cost-effectiveness, prolonged cycle life, satisfactory energy density, and enhanced safety features [10]. The inherent stability of LFP batteries, even under harsh operating conditions, devoid of environmentally concerning materials like cobalt [11], makes them an appealing option also for car manufacturers eyeing affordable and well-accepted mobility solutions.

Yet, choosing the appropriate battery chemistry is merely one facet of EES planning. Equally vital, though sometimes overlooked, is the implementation of a suitable diagnostic platform, specifically the Battery Management System (BMS). The BMS plays a central role in ensuring safety, especially under challenging conditions, and in the accurate estimation and control of the battery system [12]. Precise State-of-Charge (SOC) estimations in an EES setup are imperative, aiding in the prevention of over(dis)charging and laying the groundwork for advanced energy management strategies allowing high availability of the system, which is necessary for cost-optimized operation [13]. Nevertheless, the inherent characteristics of LFP, such as its pronounced nonlinear behaviour due to large voltage plateaus and associated hysteresis in combination with steep OCV only at very low and very high SOCs, challenge conventional diagnostic methods around Coulomb counting [10,14]. This is particularly the case in the context of applications with rare full charge or discharge conditions, such as in frequency control reserve or mild hybrid vehicles, since these methods rely on the lookup of the SOC–OCV relationship to compensate unavoidable integration errors [13–15].

To address these challenges with the diagnostics of LFP battery systems, a variety of algorithms and modelling techniques have been proposed and investigated in the literature. Table 1 provides a detailed outlook on the available literature around the topic of hysteresis modelling and SOC estimation of various lithium-based chemistries. From the literature, it is evident that predominantly applications in electromobility are researched whose constraints are not universally applicable due to significant differences in the application scenario of e.g. LSS or 48 V mild hybrid electric vehicles (HEV) [13,16,17], as detailed in Section 4. Additionally, modelling hysteresis of lithium battery's OCV for SOx estimations has not been focused for real-life implementations of BMS due to its known complexity. Utilizing the various mentioned modelling techniques in Table 1 variety of SOC estimation algorithms are available in literature namely, variants of Kalman Filters (EKF, UKF, AEKF, DUKF) [18,19], H-infinity filter (HIF) [20] and particle filters (PF) [21]. Meanwhile authors of [22–24] employ optimized versions of recursive least-squares algorithms in their approaches to dynamically estimate the model parameters for improved SOC estimation. Lastly, with gaining popularity, machine learning techniques such as support vector machine [25], deep neural network [15] and recurrent neural network [14,26] have also been proposed. Such machine learning techniques are employed mainly to accurately model the complex non-linearity of the SOC–OCV relationship.

In addressing the diagnostic challenges associated with LFP and similar cell chemistries for LSS operated in the frequency containment reserve (FCR) market, this study provides the following main contributions:

- Demonstration of seamless incorporation of a simplified hysteresis model into an RC-based battery model, priming it for integration within modern BMS frameworks.
- Showcasing the integration of the hysteresis model into different model-based SOC estimation approaches, and evaluating the resulting accuracy and robustness of the estimators in a very challenging application scenario for the BMS.
- Presenting, testing and validation of selected SOC estimation algorithms under multiple but identical conditions of a frequency containment reserve LFP battery application, set by a sophisticated Model-in-the-loop toolchain, in order to enable comparable and realistic conclusions.
- Offering a forward-looking perspective on model-based SOC estimation tailored for cell chemistries echoing LFP traits — predominantly the flat OCV curve and pronounced OCV hysteresis, to enable the broad application of knowledge gained.

The paper is structured as follows. At first, an introduction to LFP characteristics is given in Section 2 and the proposed modelling techniques as per [10,41] are explained. Second, in Section 3, a general overview of common SOC estimation algorithms in literature is given, and the considered SOC estimation algorithms are studied in detail. In Section 5, the whole system setup is briefly explained. Following this, in Section 6, the results from various experiments are evaluated to determine the optimal choice of an SOC estimation algorithm. Finally, in Section 7, a theoretical analysis is carried out to analyse if other chemistries with similar characteristics to LFP could also benefit from the proposed SOC estimation setup.

2. Characteristics of LFP and approaches to modelling

Introduced in 1997 by Professor John B. Goodenough, $LiFePO_4$ exhibits an olivine-type crystallographic structure, which inherently is more stable than the spinel structure found in other cathode materials, creating high intercalation/de-intercalation reversibility [11]. As depicted in Fig. 1(a), LFP showcases a flat OCV characteristic compared to other chemistries. A theoretical explanation as per [42] could be described as a *'two-phase'* transition process where the surface concentration of lithium ions is almost the same during both intercalation and de-intercalation processes, resulting in a flat potential. Such characteristics pose a major challenge to SOC estimation techniques, as the observability of change in SOC concerning OCV is very low. Additionally, as depicted in Fig. 1(b), one can observe the presence of a pronounced hysteresis in the OCV of LFP especially with respect to the low voltage gradient, which is mainly attributed to thermodynamic

Table 1
Taxonomy table of recent literature aiming to assess the hysteresis effect of various battery chemistries.

Ref.	Modelling technique	Applicability in BMS	Cell chemistry	Application aimed
[27]	n^{th} order RC model + hysteresis unit	Yes	LFP	
[18]		Yes	NMC	EV
[28]		Yes	LiMnO	
[20]		Yes	LiPo	
[29]		Yes	NMC	Experimental
[30]		Yes	LFP	
[31]		Yes	LFP	2nd life/LSS
[32]	Preisach model + hysterons to produce the hysteresis effect	No	NMC	Experimental
[33]	n^{th} order RC model	No[a]		EV/experimental
[34]		Yes		LSS
[35]		Yes		HEV
[19]		Yes	LFP	EV
[36]		Yes		Experimental
[37]	Multi-sensor fusion	Yes		EV
[14,15,38–40]	Machine learning techniques	Yes[b]		EV

LiPo: Lithium Polymer, LiMnO: Lithium Manganese Oxide, NMC: Lithium Nickle Manganese Cobalt, LFP: Lithium Iron Phosphate, LSS: Large scale storage system, EV: Electric Vehicles, HEV: Hybrid Electric Vehicles.

[a] Authors propose acquiring model parameters with ultrasonic experiments, which could be a costly BMS implementation.

[b] When externally trained.

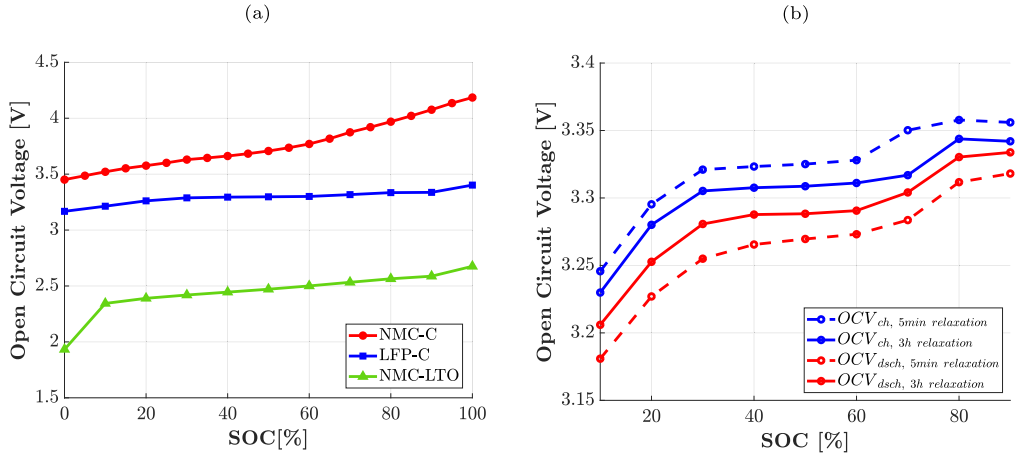

Fig. 1. Characteristics of LFP: (a) depicts OCV flatness compared to other chemistries, and (b) represents OCV hysteresis (between 10%–90% SOC) measured after two relaxed conditions, i.e. after 5 min and 3 h based on [10].

effects and mechanical stress within the electrodes [42]. In practice, the observed hysteresis behaviour is furthermore affected by comparably long relaxation time constants, temperature influence and significant changes in shape due to the ageing of the cell [10]. Thus significantly increasing the system's nonlinearity and making voltage model-based SOC estimations more difficult.

While the gradient of the OCV curve remains an intrinsic characteristic that is beyond external control, the impact of hysteresis on model-based SOC estimation can be mitigated through the employment of an OCV hysteresis model. An exemplar of such a model has been outlined by [10], as described subsequently.

$$OCV(SOC,\Psi) = \Psi \cdot OCV_{CH}(SOC) + (1-\Psi)\cdot OCV_{DCH}(SOC) \tag{1}$$

$$\Psi = \begin{cases} 0, & g < 0 \\ g, & 0 \le g \le 1 \\ 1, & g > 1 \end{cases} \tag{2}$$

$$g = \sum_{i=1}^{n} m_{ii} \int \frac{m_i \cdot I_{cell}}{C_{nom}} dt, \quad \text{where } n > 0 \tag{3}$$

The OCV at any given point in time can be represented as a function of SOC and Ψ as defined in Eq. (1), where OCV_{CH} and OCV_{DCH} depict the charging (CH) and discharging (DCH) boundaries of the OCV obtained from lab experiments, respectively. As defined in Eq. (2), Ψ is a factor depicting the position of the OCV during the transition from CH to DCH boundaries or vice versa. Ψ is calculated as per the variable g, which in turn is dependent on the current through the cell, i.e. I_{cell}, having a nominal capacity C_{nom}, also defined in Eq. (3). As depicted in Fig. 2, Ψ ranges from 0 to 1, where 0 indicates the OCV is at the discharge boundary and 1 indicates the OCV is at the charge boundary. The variation of Ψ depends on the amount of charge transferred by the current profile and is depicted as per Eq. (2). The factors m_{ii} and m_i are obtained after multiple minor loop testing and curve fittings at laboratory conditions. It is clear from Eq. (3) that with a larger value of n, i.e., with a higher number of integrals, the accuracy increases, but at the cost of higher computation load [10]. To minimize the computational effort on the BMS, n is set to 1 in this work.

For the cell used for experimental validation as defined in Section 5, 1st to 4th order of Thevenin models were used to fit the Electrochemical Impedance Spectroscopy (EIS) measurements, of which 3rd and 4th order provided good and similar results. Thus, to keep the modelling precision high, and also the computational cost low a 3rd order battery model as shown in Fig. 3 is used in this work. Here, R_0 models the

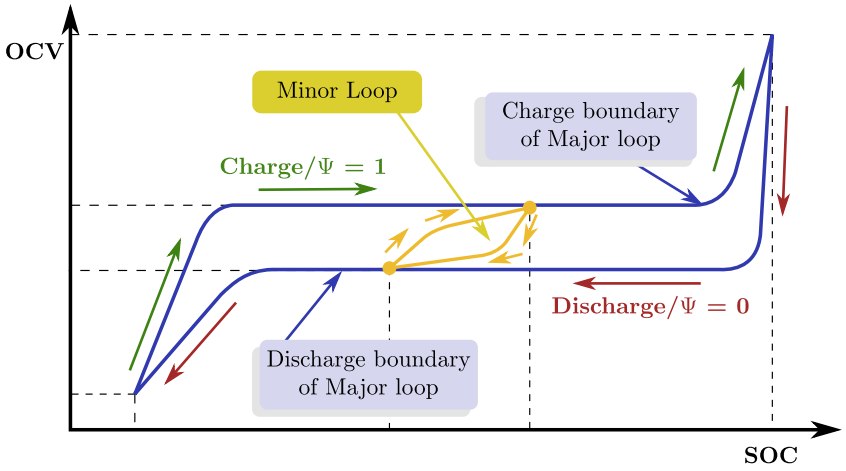

Fig. 2. Representation of major and minor loops in OCV hysteresis model.
Source: Based on [10].

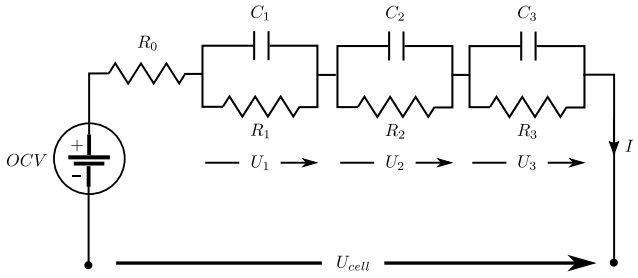

Fig. 3. 3rd-order RC battery model, with OCV, ohmic resistance R_0, resistances of the RC network R_1, R_2 and R_3 and capacitances of the RC network C_1, C_2 and C_3.

ohmic resistance and the 3 RC elements in series with short to long time constant respectively model the polarization over-voltages. Based on Coulomb counting and the linear differential equations of RC circuits, the discrete-time dynamic equations of the cell model and cell voltage are expressed by Eqs. (4), and (5).

$$SOC(k) = SOC(k-1) + I(k) \cdot \Delta t / C_{\text{nom}} \tag{4}$$

$$U_{cell} = OCV(SOC(k), \Psi(k)) + I(k) \cdot R_0 + U_1(k) + U_2(k) + U_3(k) \tag{5}$$

In reference to Fig. 3 and denoting $I(k)$ as the input ($u(k)$) to the model with positive values of $I(k)$ corresponding to charging the battery, and U_{cell} as the output ($y(k)$), the state vector of the system x_k is chosen as

$$\mathbf{x}_k = [SOC, U_1, U_2, U_3]^T \tag{6}$$

Thus, the whole system could be represented as Eq. (7), which also facilitates usage in model-based estimation methods discussed in the next section.

$$\mathbf{x}_k = \mathbf{A} \cdot \mathbf{x}_{k-1} + \mathbf{B} \cdot u_k \tag{7}$$

and

$$\mathbf{y}_k = g(\mathbf{x}_k, u_k) \tag{8}$$

where **A** is the dynamic matrix, **B** is the input matrix and g(·) is the non-linear process output model.

3. SOC estimation algorithms

The primary and most common method of estimating the SOC is using a Coulomb counting approach, which samples the battery current and computes the accumulated charge and discharge to finally estimate the SOC [43–45]. Although such a method is simple and inexpensive to implement, it faces the drawbacks of high dependence on the initial SOC accuracy and accumulated error over time due to measurement inaccuracies. While obtaining an accurate initial SOC value is possible under lab conditions, measurement errors are inevitable in a real-life scenario [46]. OCV-based approaches of SOC estimation are typically used to solve the problem due to accumulative errors, wherein the SOC is reset to a known value according to the OCV–SOC relationship. As also explained in Section 5, this is not feasible for stationary storage applications, such as primary control reserve, as there are no suitable relaxation pauses in power requirement where the measured voltage could be approximated as OCV. Especially in the case of LFP, as discussed earlier, such a method will not be meaningful in a wide range of SOC, as the OCV barely changes during most of the SOC range, thus providing little to no information of change in SOC [10]. Furthermore, advanced SOC estimation algorithms pertain to model-based techniques, namely: Luenberger observers [47,48], Kalman Filtering [48–57], Particle filtering [58,59] and others. These methods obtain the SOC using Coulomb integration but, at the same time, are self-corrected with the error between model-based cell voltage estimation and measurements. Of these, Kalman filters specifically have been researched a lot mainly because of their computational simplicity, estimation accuracy, fast cumulative error mitigation, and modularity, which enables them to be adapted for high accuracy under various degrees of non-linearity.

As described in Section 2, an LFP battery is a highly non-linear system. Therefore, higher-order model-based estimations are typically a good choice. Thus, three model-based non-linear filtering methods were implemented and tested in this work, namely: Extended Kalman Filter (EKF), Dual Unscented Kalman Filter (DUKF), and Particle Filter (PF). The underlying principle of operation for all the methods mentioned is the same, i.e., correction of states estimated using the difference between the measured and estimated output voltage. The differences in the functionality of the algorithms are described as follows:

3.1. Extended Kalman filter

The EKF is widely used in industry due to its simplicity and low computation cost [60]. The term *'Extended'* in EKF refers to the linearization process of the non-linear input system. EKF is preferred for systems with lower non-linearity, as the non-linearity is linearized only with the first order of the Taylor series expansion [61]. Nevertheless, since an OCV hysteresis model is used in the battery model for this work, it is interesting to analyse to which degree it reduces the system's

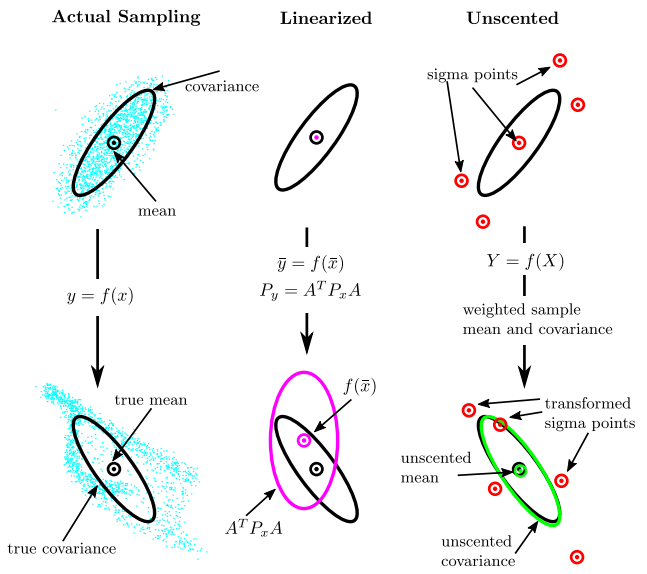

Fig. 4. Operational differences between an EKF and UKF (i.e. using sigma points). *Source:* Based on [49].

nonlinearity and thus makes the EKF an acceptable estimator. Following the linear state space description in (7) and (8), the considered state space is as follows:

$$\mathbf{x}_k = \mathbf{A} \cdot \mathbf{x}_{k-1} + \mathbf{B} \cdot u_k + \mathbf{w}_k \tag{9}$$

and

$$\mathbf{y}_k = g(\mathbf{x}_k, u_k) + \mathbf{v}_k \tag{10}$$

where vector $\mathbf{w}_k$ and $\mathbf{v}_k$ are system and measurement noise, respectively. Both $\mathbf{w}_k$ and $\mathbf{v}_k$ are assumed to be uncorrelated, zero-mean Gaussian white noise and their covariances are known as $\mathbf{Q}_k$ and $\mathbf{R}_k$ respectively. In brief, the evaluation with EKF happens in two steps: 1. Time update (prediction) and 2. Measurement update (correction). The first step generates the new predicted state as per the model defined, also termed as an a priori state estimate ($\hat{\mathbf{x}}_k^-$). In the second step based on the measured output and the predicted output from $\hat{\mathbf{x}}_k^-$, Kalman gain is calculated. This is then further used to calculate the corrected state of the system, also termed as post-priori state estimate ($\hat{\mathbf{x}}_k^+$). Please refer to [50] for detailed equations.

3.2. Sigma point Kalman filter

The Sigma Point Kalman Filter (SPKF) or Unscented Kalman Filter (UKF) enhances the linearization process by using deterministically spaced state estimates ($\mathbf{X}_{k-1}^+$), so-called sigma-points, as shown in Fig. 4. This enhances the linearization until the third-order of the Taylor series expansion [49], which makes it more accurate but significantly increases the computational cost in comparison to EKF.

The sigma points are located at the mean and symmetrically along the main axes of the covariance and are calculated as per G. L. Plett in [51]. The total number of sigma points $\mathbf{X}_{k-1}^+$ calculated at every iteration is $2N + 1$. In this work N is 4, as defined in (6), thus the total number of sigma points is 9. The overall process of evaluation is similar to that of an EKF as defined in Section 3.1 and follows [51].

To address the high non-linearity of the LFP system and to provide a more sophisticated alternative to the EKF for this study, a DUKF is used as also described in [51]. In this system, both states ($\mathbf{x}_k$ as defined in (6)) as well as model parameters ($\boldsymbol{\theta}_k$) are estimated simultaneously with two UKFs (see Fig. 5). In our case the second UKF responsible for estimating the model parameters estimates only the internal resistance R_i and rest, i.e. C_i and R_0 are kept constant. Although there are two UKFs implemented in this setup, the computational cost is nearly the same as the case of a single UKF [51]. Such a system is more robust and precise, as both the filters complement each other in different time scales (states in minutes to hours, parameters in months to years) and, over time, reduce errors due to model parameters as well as states.

As shown in Fig. 5 and detailed in [51], both filters are coupled to each other, wherein the estimated states are fed to the parameter filter and vice versa. It is important to note that only the priori parameter estimate ($\hat{\boldsymbol{\theta}}_k^-$) is sent to the state filter, whereas post-priori states ($\hat{\mathbf{x}}_{k-1}^+$) are sent to the parameter filter. For this, the time update of the state filter is modified as:

$$\hat{\mathbf{X}}_k^* = f(\mathbf{X}_{k-1}^+, \hat{\boldsymbol{\theta}}_k^-, u_k, \bar{\mathbf{w}}_{k-1}, k-1) \tag{11}$$

and similarly, for the parameter filter, it would be:

$$\hat{\mathbf{D}}_k^* = f(\hat{\mathbf{x}}_{k-1}^+, \mathbf{W}_{k-1}^+, u_k, \bar{\mathbf{r}}_{k-1}, k-1) \tag{12}$$

where $\hat{\mathbf{D}}_k^*$ are the predicted updates of the sigma points, $\mathbf{W}_{k-1}^+$ are the parameter sigma points and $\bar{\mathbf{r}}_{k-1}$ is the process noise in case of the parameter filter. Unlike the state filter, the parameter filter's prediction update step is as follows:

$$\hat{\boldsymbol{\theta}}_k^- = \hat{\boldsymbol{\theta}}_{k-1}^+ \tag{13}$$

For more detailed equations of parameter filter and state filter in a DUKF please refer to [51].

3.3. Particle filter

Kalman filtering methods, as described above, are based on Gaussian distributions. In contrast, Particle Filters (PF) employ Monte Carlo-based sampling techniques. This gives the PF the advantage to deal with any kind of distribution by approximating the respective probability density function of samples, or in other words, particles [59]. For a highly non-linear system such as LFP, PF can provide good performance with SOC estimation [59]. Similar to the Kalman filter, PF also works with the same state space representation as defined in (9) and (10). The PF process is implemented as by Schwunk et al. [59] and can be summarized as follows:

- Particle generation
  Unlike, mathematically calculating the sigma points in the UKF, the particles initialized in this step, are randomly distributed with the previously estimated value as the seed. Instead of using a Gaussian distribution, the Cauchy Lorentz distribution is employed in this work. As illustrated in Fig. 6, the Cauchy–Lorentz distribution enhances the robustness of the Particle Filter (PF) owing to its heavy-tailed nature compared to the Gaussian distribution. This characteristic effectively mitigates the issue of sample impoverishment [59,62,63]. Cauchy's Probability Density Function is generated as [59]:

  $$\mathbf{PD} = \mathbf{P}_k \cdot \tan(\pi(rand(\mathbf{M}, 1) - 0.5)) \tag{14}$$

  where $\mathbf{M}$ is the number of particles to be generated and must always be $\mathbf{M} > 0$, and $\mathbf{P}_k$ is the set of variance for random particle distribution. With a given $\mathbf{PD}$ the particles are generated as follows:

  $$\mathbf{X}_{k-1}^{+\,[i]} = \hat{\mathbf{x}}_{k-1}^+ + \mathbf{PD}, \quad i = 1, 2, \ldots, M \tag{15}$$

- Time update (prediction)
  Similar to prediction step of EKF, a priori state ($\mathbf{X}_k^*$) of for every particle from i = 1,2, …, $\mathbf{M}$ is generated through the model defined in Eq. (9).
- Measurement update
  Every ith predicted particle is used to predict the output ($\mathbf{Y}_k^*$) as per Eq. (10), which is later used for comparison with the measurement.

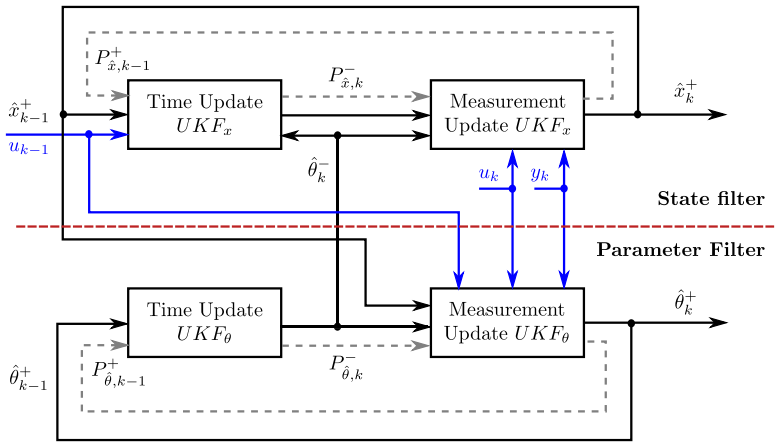

Fig. 5. Block diagram of DUKF with state and parameter filters coupled to each other. Signals for coupling are in blue.
Source: Adapted from [51].

- Determine Particle weights
  In this step, the likelihood of the ith particle is calculated with the equation:

$$\mathbf{q}_k^{[i]} = exp\left(-\frac{1}{2\sqrt{\mathbf{R}_k}}(\mathbf{y}_k - \mathbf{Y}_k^*)^2\right) / \sqrt{2\pi\mathbf{R}_k} \tag{16}$$

  where $\mathbf{y}_k$ is the actual measurement at step k. Then $\mathbf{q}_k^{[i]}$ is normalized for each particle by:

$$\boldsymbol{\omega}_k^{[i]} = \frac{\mathbf{q}_k^{[i]}}{\sum_{j=1}^{M} \mathbf{q}_k^{[j]}} \tag{17}$$

  where $\boldsymbol{\omega}_k^{[i]}$ is the normalized weight for the ith particle. In other words, $\boldsymbol{\omega}_k^{[i]}$ represents the probability of observing the measurement from the corresponding particle's state.
- Re-sample
  This is one of the most crucial steps of PF in terms of computational cost. All the predicted particles are re-sampled or qualitatively selected based on the weights calculated in the previous step. In this work, a Low Variance resampling method is used as defined in [64] and explained as a pseudo-code in (18). λ, U, c and i are internal variables and $\bar{\mathcal{X}}_k$ is the resampled output:

$$\begin{aligned}
&\lambda = rand(0, \mathbf{M}^{-1}), \quad c = \omega_k^{[0]}, \quad i = 1, \quad \bar{\mathcal{X}}_k = [\,] \\
&for \quad m = 1 : \mathbf{M} \; do \\
&\quad U = \lambda + (m-1) \cdot M^{-1} \\
&\quad while \quad U > c \\
&\quad\quad i = i + 1 \\
&\quad\quad c = c + \omega_k^{[i]} \\
&\quad end \; while \\
&\quad add \; \mathbf{X}_k^{*[i]} \; to \; \bar{\mathcal{X}}_k \\
&end \; for \\
&return \; \bar{\mathcal{X}}_k
\end{aligned} \tag{18}$$

- State estimation
  Finally, the average of the resampled states is the estimated (or post priori) state.

$$\hat{\mathbf{x}}_k^+ = \frac{1}{\mathbf{M}} \sum_{i=1}^{\mathbf{M}} \bar{\mathcal{X}}_k^{[i]} \tag{19}$$

4. Application scenario

Unlike many other works that focus on batteries in electric vehicles, in this study we focus on a LSS application. Specifically, we have chosen a 5 MW stationary energy storage system (M5Bat [13,65,66]), operated in the FCR market [4] and located in Aachen, Germany, as an example. The operating profile utilized for this study was recorded in the field in January 2019 and is depicted in Fig. 7 as a scaled-down representation adapted to the capabilities of a single LFP cell under study. The corresponding data is available at [67].

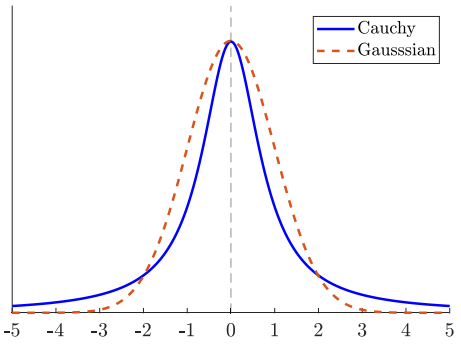

Fig. 6. A qualitative comparison between Probability Density Function (PDF) of Cauchy and Gauss distribution.

In contrast to electric vehicles or home energy storage systems, as can be seen in Fig. 7, the FCR function in the energy grid leads to operation without pauses or constant charging regimes [4]. In addition, due to regulatory measures in this operation, the SOC window is limited to a range between 20 and 80% SOC or even less [4]. As a result, this application excludes almost all operating points at which a recalibration of the SOC estimator would normally take place [15,43]. Hence, the diagnostic algorithms for such systems must exhibit exceptional robustness and online precision to handle these kinds of errors until a rare and expensive maintenance break [13]. From a diagnostics perspective, this use case can therefore be considered a worst-case scenario, especially when using LFP batteries.

5. Model-based validation environment

The architecture of a BMS is multifaceted, comprising components such as sensors, filtering circuits, data acquisition systems, and diagnostic as well as control algorithms. In this study, we employ a Model-in-the-Loop (MiL) toolchain, previously outlined in [68] and illustrated in 8. This toolchain replicates each of these components to study their individual and collective impact. A critical component of the toolchain is the High Precision Reference Battery Model (HPRM), which accurately mimics an actual battery's voltage, temperature, and other key characteristics like SOC, OCV, and polarization voltages through a physically motivated high-order electrical equivalent circuit

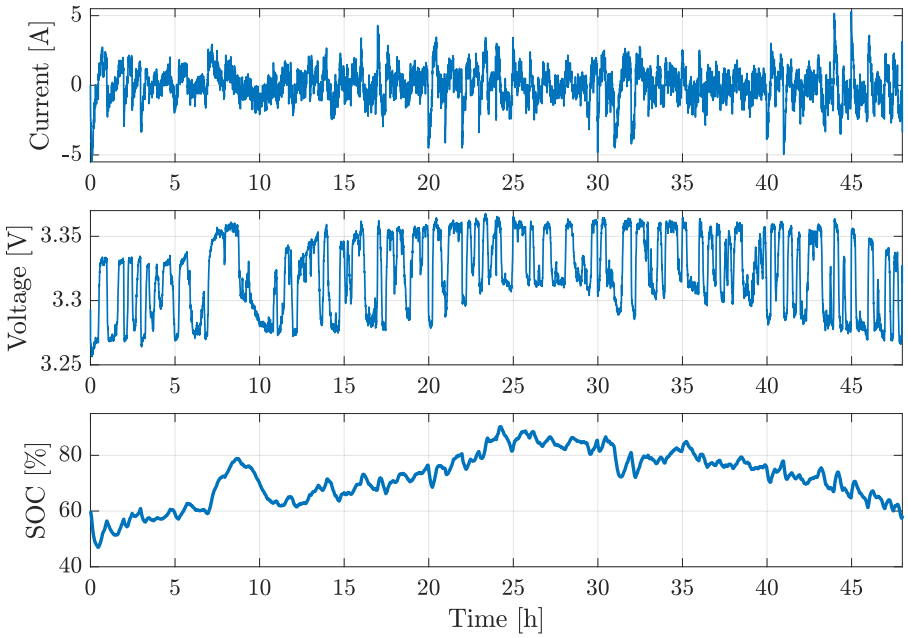

Fig. 7. Grid primary reserve application profile recorded at M5Bat [66] in January 2019, with voltage and SOC response emulated by HPRM of an LFP cell. The corresponding data is available at [67].

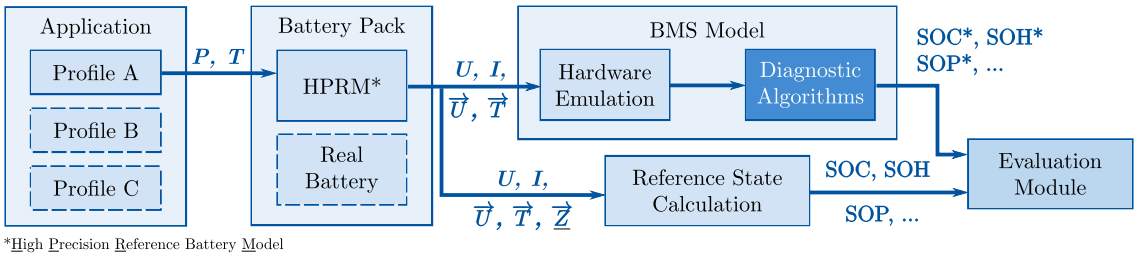

Fig. 8. Model-in-the-Loop toolchain with an application model, high precision reference battery model, and BMS model.

model [10,69]. By using such a model instead of direct measurement data from cells, it is possible to accurately know the reference states that cannot be measured directly.

The reference model in this study is configured to emulate an 8 Ah high-power LFP cell, specifically the OMTLIFE8AHC-HP from OMT GmbH, investigated and characterized in chapter 5 of [10]. BMS functionalities are realized through a MATLAB/Simulink-based model, being responsible for computing all reference state variables, including SOC, SOH, and SOP. The toolchain allows to be configured for various application scenarios, for this study it replicates the LSS application with FCR operation described in 4, which is permanently close to room temperature due to air conditioning. In the scope of this work, we concentrate primarily on exploring the particularly challenging application scenario and delve into the influence of hysteresis modelling on diagnostic accuracy and robustness in such a scenario. Due to the complexity and the extensive range of parameters and simulations required to thoroughly investigate the effects of ageing and temperature on SOC estimation, we have decided not to include an analysis of these aspects in this study, even though we are aware of the importance of understanding these factors. Accordingly, all analyses were performed at 100% SOH and 25 °C.

To assess the considered SOC estimation methodologies, they are executed under exactly the same operating conditions, including temperature and sensor inaccuracies. The SOC obtained from the HPRM is considered the reference value while evaluating the outcome of the SOC estimation algorithms. The MiL toolchain also enables the manipulation of operating conditions, allowing the algorithms' performance to be evaluated under varying SOC initializations and sensor errors. Subsequent analysis focuses on key performance indicators such as estimation convergence rate, accuracy, computational cost, and the robustness of the algorithms, which are elaborated upon in Section 6.

6. Results and discussions

6.1. SOC estimation performance comparison

Fig. 9 demonstrates the results of the proposed estimation approaches, i.e. EKF, DUKF and PF (with 100 particles, $\mathbf{M} = 100$). The corresponding data is available at [67]. Each estimation approach is falsely initialized to 50% SOC, whereas the actual start SOC was 60%. The load profile described in Section 5 extends over two days. This longer period for evaluation allows to collect enough data to support the findings properly.

SOC tracking and estimation error

The SOC tracking, displayed in Fig. 9(a), indicates that both the DUKF and the PF perform well in tracking the reference SOC. Whereas the EKF starts to deviate after a certain period. This is apparently due to the fact that EKF has limited linearizing capability [61], which is outplayed by the heavy non-linearity caused due to LFP's OCV gradient and hysteresis. Although in this work a hysteresis model has been integrated into the battery model to reduce such non-linearity, EKF could not sufficiently benefit from this.

Fig. 9(b) gives a clearer view of the SOC estimation error recorded by individual approaches during the whole simulation. The estimation

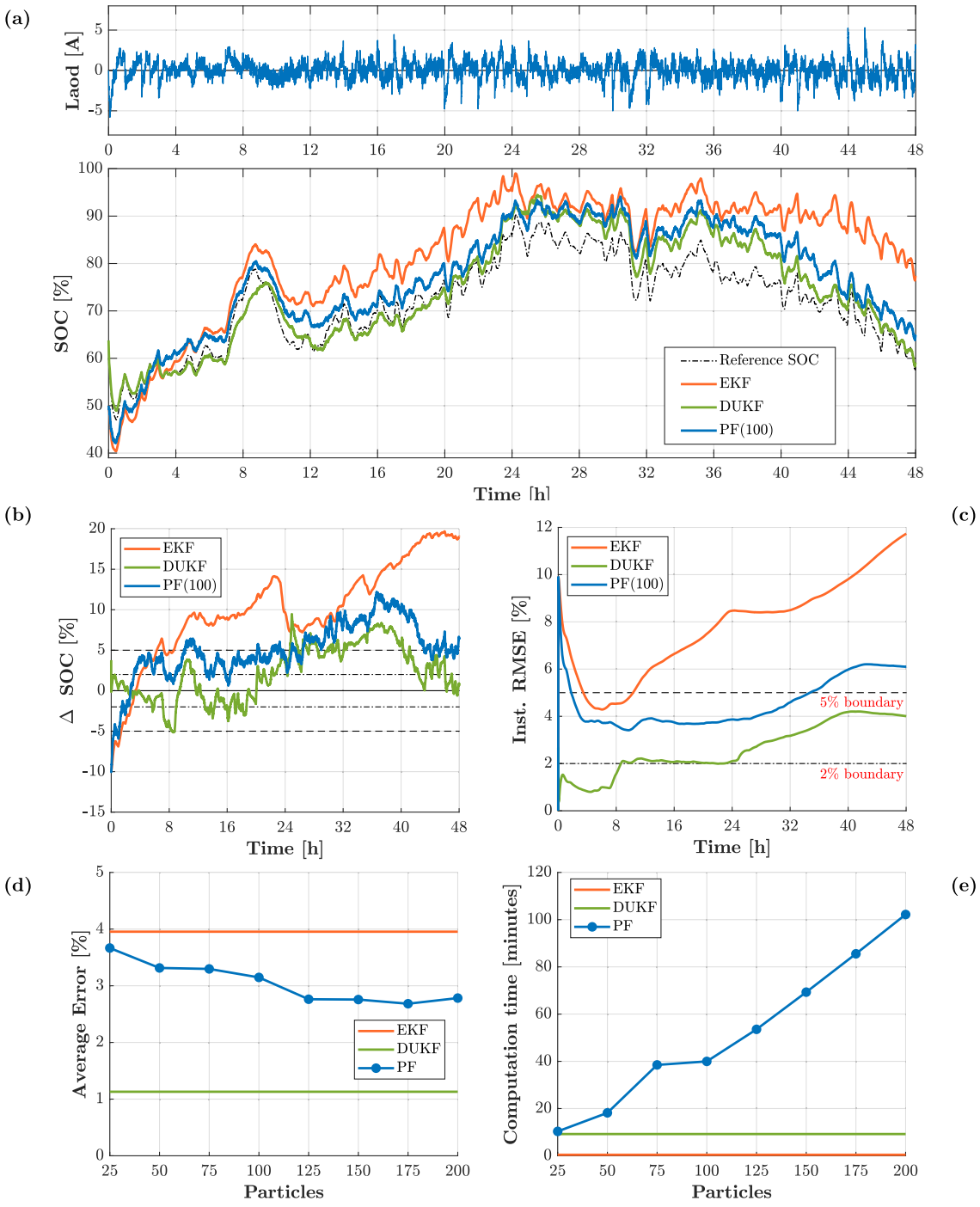

Fig. 9. Results of the model-in-the-loop tool chain simulation for the primary control reserve application profile spanning 2 days. (a) Comparison of SOCs estimated from three different algorithms against the reference SOC calculated by the HPRM. (b) Comparison of error between the estimated and reference SOC values, with boundaries of ±2% and ±5%. (c) Root Mean Square Error comparison over time, with 2% and 5% error boundaries. (d) Comparison of estimation performance of EKF, DUKF and PF with various particles. (e) Comparison of computational performance in terms of computation time on the same PC under the same load.

error is calculated as per Eq. (20).

$$\Delta SOC\ [\%] = Estimated\ SOC\ [\%] - Reference\ SOC\ [\%] \tag{20}$$

From the figure, it is evident that the implemented DUKF is comparably fast in converging to the reference SOC and at the same time, stays within acceptable error limits of ±5%. Interestingly, both DUKF and PF have greater error values at higher SOC values, i.e. around 80%–90% SOC. This behaviour is probably due to modelling inaccuracies that are usually difficult to compensate for in very high or low SOC areas. Since the DUKF consists of two KFs, one of which estimates the cell's internal resistance, it is capable enough of reducing such modelling issues, thus resulting in a higher estimation performance compared to the PF.

Instantaneous Root Mean Square Error

The Root Mean Square Error (RMSE) is the standard deviation of the estimation errors. To understand the dynamics of change in squared error at every point, the instantaneous RMSE value is proposed as a performance evaluation factor, as available in Fig. 9(c). The instantaneous RMSE value is the evolution of the RMSE for the whole test. Thus it

can be defined as per Eq. (21).

$$inst.\ RMSE = [0,\ RMSE_{t_1\ to\ t_2},\ RMSE_{t_1\ to\ t_3} \dots,\ RMSE_{t_1\ to\ t_n}] \quad (21)$$

where

$$time = [t_1,\ t_2,\ t_3,\ \dots\ t_n]$$

As evident in the figure, once the system starts entering a higher SOC range, both DUKF and PF start deviating from their steady states, but DUKF maintains a lower error level compared to the PF.

Average error

It is fair to say that a higher number of particles in a PF could lead to increased accuracy. Thus, results from different setups, i.e. varying numbers of particles in the PF, are compared with the results of EKF and DUKF. Fig. 9(d) showcases the average error recorded for EKF, DUKF, and PF. In this scenario, only estimation errors recorded *after* the first 10 min from the start of the profile are considered. This period is assumed to be sufficient for the estimators to converge to the actual value and to meet the requirements of the application. Fig. 9(d) demonstrates that the estimation accuracy enhances with a rising number of particles; however, this is accompanied by an increased computational demand. Notably, the enhancement in performance reaches a plateau at approximately 125 particles.

Computational cost

Fig. 9(e) shows the simulation time for the complete simulation on the same personal computer under the same computational load. From the figure, it is clear that the computation time of the PF increases nearly linearly to the increased number of particles. But, the most crucial point to note is that the computation cost of the PF is always higher than for the DUKF while still being less accurate than the DUKF.

6.2. Robustness testing

The simulation results presented above show the performance of the SOC estimators under defined states and initializations. For a method to be used in real-life applications, an SOC estimator must be able to suppress all the system uncertainties and disturbances, which is ensured by robustness testing [70].

One of the primary system-level uncertainties is the setup of the estimators themselves, i.e. implementations, initializations and tuning parameters. System-level initializations such as SOC, offsets, and over-voltages play a significant role in determining optimal tuning parameters. Thus poor initializations could also lead to improper tuning of the SOC estimators [43]. Therefore, robustness testing in terms of different SOC initializations was carried out with the first 8 hrs of the load profile from M5Bat discussed in Section 5, results of which are shown in 10(a) and the data being available at [67]. From this robustness analysis, it is evident that the DUKF converges to the reference SOC value irrespective of how the system is initialized, thus showcasing its superiority in performance. EKF is slow in convergence, and at the same time has poorer estimation accuracy when compared to DUKF and PF, for different SOC initializations. Also, as already discussed in the previous Section 6.1, the results tend to deviate later onwards. On the other hand, PF shows similar results to EKF, but as we saw in the previous Section 6.1, it has a better tracking behaviour compared to EKF.

All the components in a BMS degrade over time. Thus, to sufficiently evaluate the robustness of the estimators, system disturbances due to the sensors must be considered [71,72]. Therefore, robustness analysis of all the SOC estimators (with SOC_0 = 50%) is carried out against sensor errors: gain (1.1), offset (0.1 A) and noise (10× nominal noise), observed in the current sensor. As shown in Fig. 10(b) not only the above-mentioned individual current sensor errors but also its combinations were employed in robustness testing, to investigate the behaviour of the estimators to each error. The box plot in Fig. 10(b) defines the median and overall range of estimation error recorded after the first 10 min of the load profile. As suggested in Section 6.1, this is to avoid substantial estimation errors before the system converges to the reference SOC. From the figure, it is evident that DUKF maintains well within the error limit of ±2%, irrespective of what kind of sensor error it is subjected to. PF and EKF on the other hand are able to maintain the errors within the ±5% error range. Offset error seems to be the most difficult to suppress while considering DUKF, which reflects its respective combination Gain + Offset, Noise + Offset and Gain + Offset + Noise as well. Overall, it can be concluded from the robustness testing that the DUKF has the best performance under real-life conditions.

7. Potential application on other chemistries

Building on the research surrounding LFP batteries, this section transitions towards exploring the implications for other lithium-ion chemistries. LFP's distinctive combination of non-negligible hysteresis behaviour and a predominantly flat OCV curve has necessitated specialized diagnostic techniques, specifically model-based approaches with powerful estimators. Similar attributes can be observed in other cell chemistries, albeit with varying degrees of expression, raising the question of the generalizability of our diagnostic approaches [73].

The central objective here is to conduct a theoretical assessment of the potential applicability of the SOC estimators optimized for LFP to other chemistries. This inquiry focuses on two primary metrics. Firstly, it evaluates the voltage difference across the OCV curve between the empty and full states, specifically between 3% and 97% SOC based on our measurements. This approach excludes the steep sections that could distort the result. The evaluation then culminates in calculating the average gradient of the OCV curve. This parameter indicates SOC observability by OCV measurement with standard frontend ADCs, which have an accuracy of 1–3 mV [74]. Second, the extent of the hysteresis is compared to understand its influence on SOC observability and the impact of incorporating a hysteresis model. Finally, the voltage gradient and the hysteresis are combined, leading to a parameter of ΔSOC through hysteresis. All these values are summarized in Table 2 for easy comparison and the underlying data is available at [67]. A graphical representation can be found in Fig. 11.

In light of the application to stationary storage — this work's primary focus — this section examines other promising contenders, specifically NMC/LTO, NMC/C, NCA/C+Si, and NMC/C+Si. This comparative analysis seeks to extend SOC estimation techniques' applicability and assess their efficacy across a broader spectrum of battery chemistries. Nevertheless, it must be noted that all showcased OCV characteristics in this work are specific to the cells tested in the lab and might also vary with design parameters not investigated in this work (e.g. electrode thickness, electrolyte additives).

7.1. NMC/LTO

NMC/LTO denotes a cell chemistry with NMC cathode and lithium titanate (LTO) anode instead of the standard graphite (C) anode. A cell of 23 Ah capacity is considered for evaluation. NMC/LTO is a chemistry which still has high costs but shows brilliant C-rate capabilities (over 70 C) and cycle life performance (over 15,000 full equivalent cycles) [75]. Thus, it enables ultra-fast charging and discharging solutions with very high cycle numbers. A major drawback, however, is the lower achievable cell voltage and, thus, lower energy density compared to the carbon-based anodes.

The OCV characteristics and its corresponding hysteresis shown by the cell are compared in 11(a). The figure shows that the overall cell voltage is much lower than for graphite anodes due to the LTO potential vs. Lithium. At the same time, the OCV curve has a certain degree of flatness but is not as flat as LFP under comparison. The change in OCV throughout the whole SOC range in LTO is ~470 mV compared to ~160 mV of LFP. Thus, the OCV curve has a certain degree of non-linearity, which implies that complex SOC estimators such as DUKF might be required. OCV characteristics not only vary with the

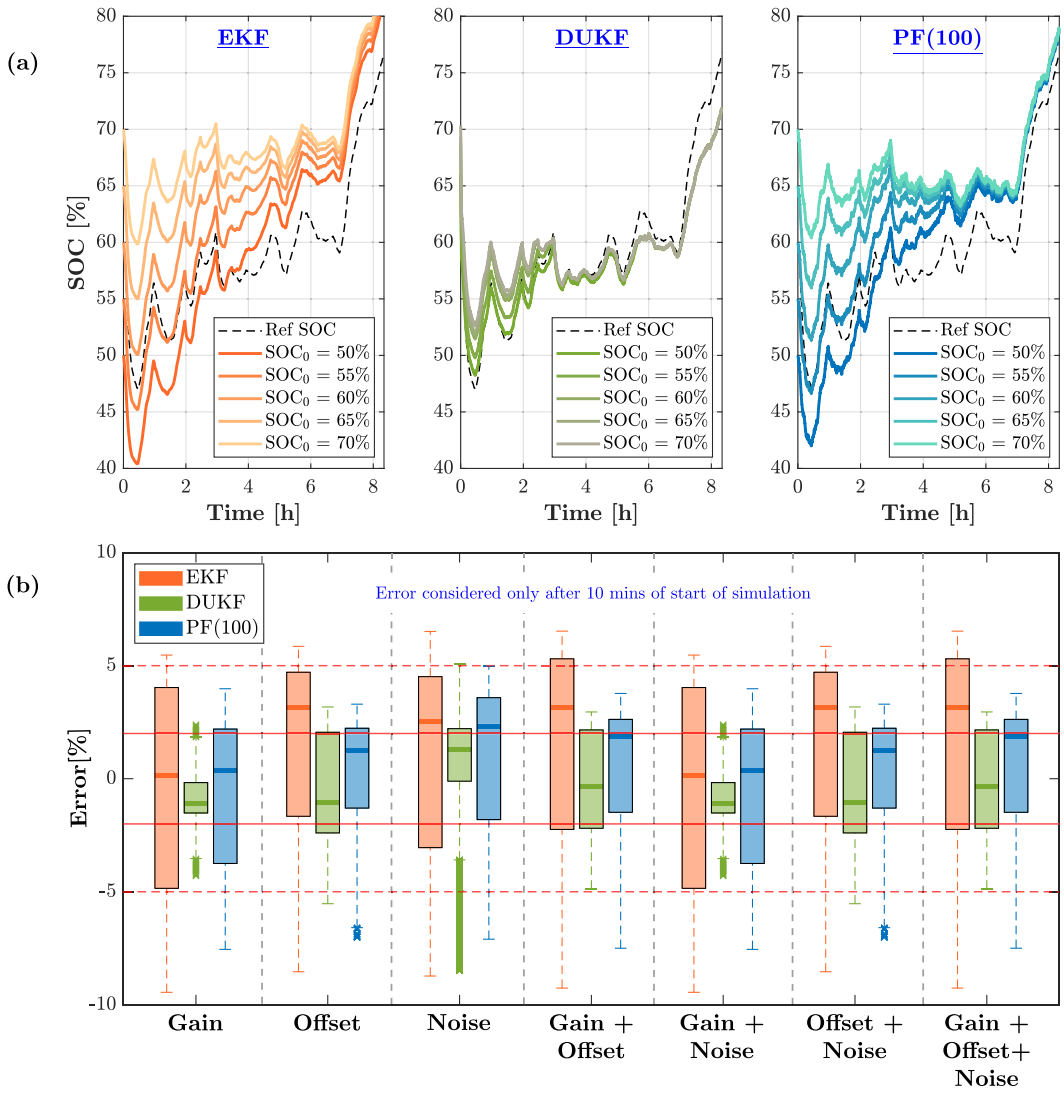

Fig. 10. Robustness testing of SOC estimation on an application of primary control reserve spanning for 8 h. (a) Robustness analysis on EKF, DUKF and PF with 100 particles for various SOC initializations. (b) Box plot of robustness testing by including artificial current sensor errors of Gain: 1.1, Offset: 0.1 A, Noise: 10×Nominal noise and its combinations.

Table 2
Comparison of the characteristics of the investigated cell types; SOC range from 3% to 97% taken into calculation.

	LFP/C	NMC/LTO	NMC/C	NCA/C+Si	NMC/C+Si
Voltage range (V)	0.16	0.47	1.01	1.27	1.21
ΔSOC per mV (%)	0.584	0.214	0.099	0.079	0.082
Mean (max) hysteresis (mV)	18.8 (27.5)	4.2 (5.7)	26.0 (65.5)	63.4 (357.0)	75.9 (302.1)
ΔSOC through hysteresis (%)	11.7 (17.1)	0.9 (1.2)	2.5 (6.5)	5.0 (28.2)	6.3 (24.9)

chemistry but also with the exact materials, manufacturing processes, and many more, as discussed in [76,77]. On the other hand, the hysteresis is remarkably low and within the accuracy of measurement and simulation. From the combination of the OCV slope and the mean hysteresis, an error in the SOC estimate of <1% (>10% for LFP) can be expected, as given in Table 2. Thus, a hysteresis model is not conducive to diagnostics for this chemistry.

7.2. NMC/C

Nickel–Manganese–Cobalt (NMC) cells with graphite anodes have emerged as a mature technology over the past decade in lithium-ion batteries. The specific cell scrutinized in this study is a 13 Ah capacity model from Kokam. The NMC/C chemistry is particularly versatile, offering several variants that adjust the proportions of Nickel (N), Manganese (M), and Cobalt (C). NMC presents a good trade-off among critical parameters such as safety, longevity, energy density, and cost [78]. Furthermore, the ability to alter the ratios of Nickel, Manganese, and Cobalt allows manufacturers to tailor the battery's properties, be it for extended lifespan or enhanced power output.

Fig. 11(b) presents a comparative analysis of the OCV curve and its associated hysteresis for the examined chemistry. Unlike LFP, the OCV curve of this chemistry exhibits an apparent gradient, indicating a lower degree of flatness. Specifically, the OCV variation spans about 1 V across the SOC range, compared to the much more limited 160 mV variation observed in LFP. Such characteristics imply that SOC estimators with limited non-linearity handling, such as the EKF, could yield satisfactory results for this particular chemistry.

The hysteresis behaviour mirrors that of LFP, albeit with slightly elevated levels compared to the measured LFP cell. However, it is essential

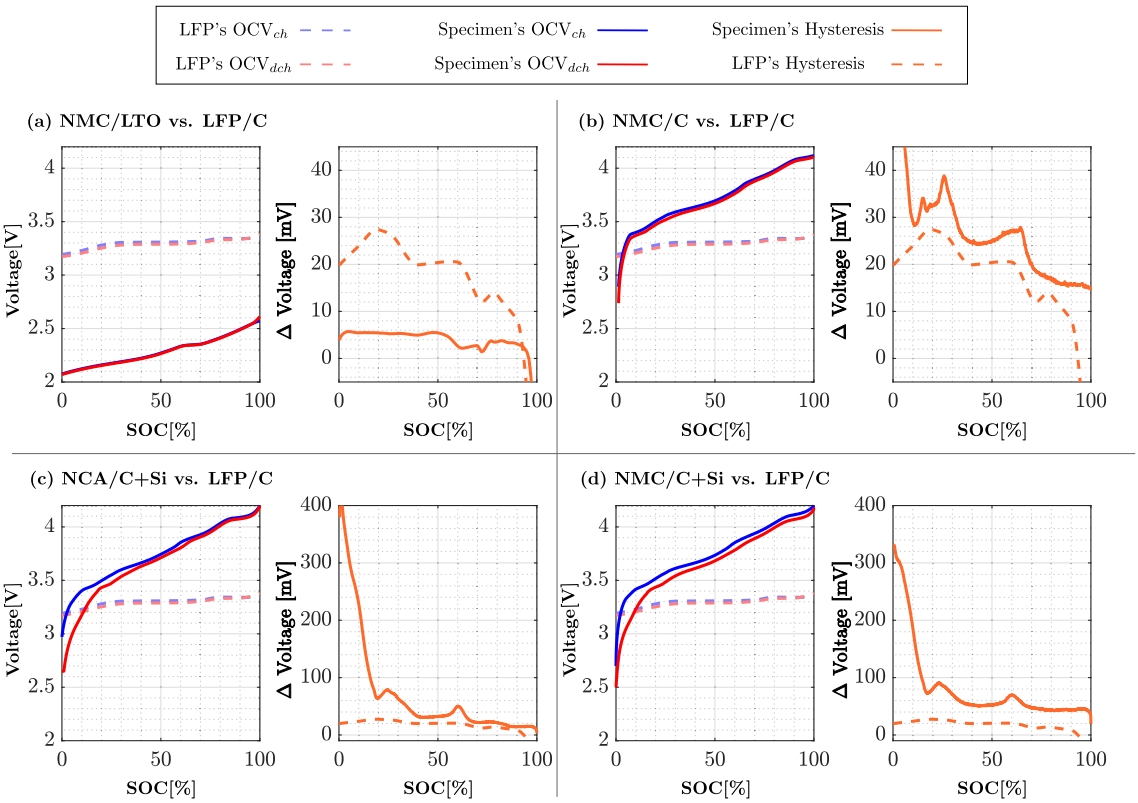

Fig. 11. OCV curve and hysteresis comparison of various chemistries to LFP. (a) NMC/C vs. LFP/C, (b) NMC/C vs. LFP/C, (c) NCA/C+Si (graphite anode doped with silicon) vs. LFP/C, (d) NMC/C+Si (graphite anode doped with silicon) vs. LFP/C.

to note that the time required for the system to reach its resting OCV is notably longer in the case of LFP. Consequently, considering both the gradient of the OCV curve and the mean hysteresis magnitude, a medium SOC estimation error of 2.5% is anticipated due to hysteresis, which is substantially lower than that generally observed for LFP.

7.3. NCA/C+Si

As an enhancement of the NCA/C chemistry, NCA/C+Si denotes a cell with an NCA cathode and a graphite anode doped with Silicon (Si). Theoretically, Si can store 3.75 Li atoms per atom of Si (when available as $Li_{15}Si_4$). Thus, the chemistry has an improved gravimetric capacity [79], which makes the chemistry an option for various high-energy applications. The cell under consideration here is a 3.5 Ah cell from Samsung (INR18650-35E).

Fig. 11(c) showcases the OCV curve and hysteresis comparison for NCA/C+Si and LFP chemistries. Notably, NCA/C+Si demonstrates a steep OCV gradient, substantially differentiating it from the flat OCV curve of LFP. The OCV variation across the entire SOC range is approximately 1.27 V for NCA/C+Si, contrasting sharply with the mere 160 mV for LFP. Such a pronounced gradient suggests that SOC estimators like the EKF, with its limited ability to handle non-linearity, could be adequate for NCA/C+Si chemistry.

The introduction of Si in the anode distinctly manifests as a strong hysteresis at low SOCs (as evident in Fig. 11(c)), confirmed by prior literature citing the mechanical stress imposed by the Si component [79–81]. The hysteresis at low SOC levels is remarkably more significant than what is typically observed in LFP. Despite this, the combination of the OCV gradient and mean hysteresis points to an anticipated SOC estimation error of around 5.0%, which is a substantial improvement over LFP. However, it is important to note that SOC estimators for NCA/C+Si could achieve improved accuracy by incorporating a hysteresis model, particularly for SOC levels below 40%. This is because the hysteresis is induced by the silicon content, meaning the SOC level at which a hysteresis model becomes beneficial depends on the silicon content in the anode.

7.4. NMC/C+Si

Similar to NCA/C+Si, NMC/C+Si features a graphite anode doped with silicon, improving gravimetric capacity and therefore augmenting its already favourable attributes of safety, durability, and cost-efficiency. For the purpose of this comparison, a 3.5 Ah cell by LG (LG INR18650MJ1) is evaluated.

Fig. 11(d) offers a comparative assessment of the OCV curve and hysteresis phenomena with LFP. At the outset, the resemblance to the attributes of NCA/C+Si, as previously discussed in 7.3, is evident. The OCV curve, spanning a voltage range exceeding 1.21 V, not only parallels the gradient of NCA/C+Si but also significantly exceeds that of LFP. Hence, conventional SOC estimators like the EKF appear to be equally effective for this chemistry. Remarkably, this chemistry exhibits the highest level of hysteresis among all the cells considered. Despite this, integrating the OCV gradient and mean hysteresis yields an estimated SOC error of 6.3%, still a considerable improvement over LFP. Consequently, the implementation of a hysteresis model can further refine the performance of SOC estimators for NMC/C+Si.

8. Conclusion

This research primarily investigates SOC estimation techniques tailored for Lithium Iron Phosphate batteries. As discussed, LFP batteries present distinctive challenges for SOC estimation. This is particularly the case in the context of applications with rare full charge and idle conditions, as investigated. The analysis carried out in this work leads to the following contributions and observations:

(i) Demanding Applications: The study has shown that there are very challenging applications for battery diagnostics outside of (H)EVs. As has been shown, these applications can also be effectively covered with appropriate state estimation approaches.
(ii) OCV Hysteresis Model for BMS: To accurately capture the hysteresis inherent in LFP, an OCV hysteresis model capable of replicating minor loops was utilized. This model adds accuracy to the model-based SOC estimation process.
(iii) SOC Estimation Algorithms: Three model-based SOC estimators with an integrated hysteresis model, namely the EKF, DUKF, and PF, were evaluated. Real-world load profiles from a LSS with FCR, served as the testbed. DUKF outperformed the other estimators largely due to its dual Kalman Filter mechanism that dynamically updates internal parameters, thereby compensating for model errors.
(iv) Robustness Testing: Validation was performed to also assess the robustness of the SOC estimators with hysteresis model. DUKF exhibited resilience in simulations with different state initializations and with the introduction of real-world sensor errors like gain, offset, and noise, thus confirming its suitability for practical applications.
(v) Other Li-Ion Chemistries: Evaluations suggest that the findings could extend to other Lithium-Ion chemistries which may also benefit from higher-order models and SOC estimators like DUKF. Further, chemistries with silicon doping in the anode, such as NCA/C+Si and NMC/C+Si, could likely gain from incorporating hysteresis models, given their strong presence at low SOCs.

As the OCV, especially in LFP batteries, is affected by ageing to a relevant extent for diagnostics, applications of the proposed diagnostic approaches should also be developed and validated in the future, taking ageing into account. This can be done, for example, by reconstructing the OCV from half-cell curves as described in [82]. Even if the influence of temperature is considered to be significantly lower, a suitable validation of the approaches should still be carried out in a relevant temperature range for the application.

The study not only addresses SOC estimation for LFP batteries but also lays the groundwork for extending the methodology to other Li-Ion chemistries. The results warrant further research, particularly in the application of these SOC estimation methods to a broader range of battery chemistries.

CRediT authorship contribution statement

Dominik Jöst: Writing – review & editing, Writing – original draft, Supervision, Software, Methodology, Investigation, Conceptualization. **Lakshimi Narayanan Palaniswamy:** Writing – original draft, Visualization, Software, Methodology, Investigation, Conceptualization. **Katharina Lilith Quade:** Writing – review & editing, Supervision, Funding acquisition. **Dirk Uwe Sauer:** Supervision, Funding acquisition, Conceptualization.

Declaration of competing interest

The authors declare that they have no known competing financial interests or personal relationships that could have appeared to influence the work reported in this paper.

Data availability

A dataset related to this article can be found at [67] (https://doi:10.18154/RWTH-2024-03667), an institutional data repository hosted at RWTH Aachen University.

Declaration of Generative AI and AI-assisted technologies in the writing process

During the preparation of this work the authors used GPT4/OpenAI in order to improve readability and language. After using this tool, the authors reviewed and edited the content as needed and take full responsibility for the content of the publication.

Acknowledgements

This work was financially supported by the German Federal Ministry of Education and Research (BMBF) within the OSLiB project (Funding Code: 03XP0330C). It was additionally supported by the European Regional Development Fund (ERDF) under the research project DUETT (Grant Number : ERDF-0800841). The responsibility for this publication rests with the authors. The authors would like to specially thank Dr. Andrea Marongiu for the substantial preliminary work in the field of LFP modelling and diagnostics at the institute [10].

References

[1] IRENA, Tracking COP28 Outcomes: Tripling Renewable Power Capacity by 2030, Report, The International Renewable Energy Agency, Abu Dhabi, 2024, URL https://www.irena.org/Publications/2024/Mar/Tracking-COP28-outcomes-Tripling-renewable-power-capacity-by-2030.
[2] IRENA, Renewable Energy Statistics 2023, Report, The International Renewable Energy Agency, Abu Dhabi, 2023, URL https://www.irena.org/Publications/2023/Jul/Renewable-energy-statistics-2023.
[3] L. Koltermann, K.K. Drenker, M.E. Celi Cortés, K. Jacqué, J. Figgener, S. Zurmühlen, D.U. Sauer, Potential analysis of current battery storage systems for providing fast grid services like synthetic inertia – case study on a 6 MW system, J. Energy Storage 57 (2023) 106190, http://dx.doi.org/10.1016/j.est.2022.106190.
[4] T. Thien, D. Schweer, D.v. Stein, A. Moser, D.U. Sauer, Real-world operating strategy and sensitivity analysis of frequency containment reserve provision with battery energy storage systems in the german market, J. Energy Storage 13 (2017) 143–163, http://dx.doi.org/10.1016/j.est.2017.06.012.
[5] T. Ioannis, T. Dalius, L. Natalia, Li-Ion Batteries for Mobility and Stationary Storage Applications – Scenarios for Costs and Market Growth, Tech. Rep., Publications Office of the European Union, 2018, http://dx.doi.org/10.2760/87175.
[6] Intergovernmental Panel on Climate Change, Summary for policymakers, in: Intergovernmental Panel on Climate Change (Ed.), Climate Change 2013 - The Physical Science Basis, Cambridge University Press, 2019, pp. 1–30, http://dx.doi.org/10.1017/cbo9781107415324.004.
[7] J. Figgener, P. Stenzel, K.-P. Kairies, J. Linßen, D. Haberschusz, O. Wessels, G. Angenendt, M. Robinius, D. Stolten, D.U. Sauer, The development of stationary battery storage systems in Germany – a market review, J. Energy Storage 29 (2020) 101153, http://dx.doi.org/10.1016/j.est.2019.101153.
[8] J. Figgener, P. Stenzel, K.-P. Kairies, J. Linßen, D. Haberschusz, O. Wessels, M. Robinius, D. Stolten, D.U. Sauer, The development of stationary battery storage systems in Germany – status 2020, J. Energy Storage 33 (2021) 101982, http://dx.doi.org/10.1016/j.est.2020.101982.
[9] P. Ralon, M. Taylor, A. Ilas, H. Diaz-Bone, K. Kairies, Electricity Storage and Renewables: Costs and Markets to 2030, International Renewable Energy Agency, Abu Dhabi, UAE, 2017, URL https://www.irena.org/-/media/Files/IRENA/Agency/Publication/2017/Oct/IRENA_Electricity_Storage_Costs_2017.pdf?rev=a264707cb8034a52b6f6123d5f1b1148.
[10] A. Marongiu, Performance and Aging Diagnostic on Lithium Iron Phosphate Batteries for Electric Vehicles and Vehicle-to-Grid Strategies (Dissertation), RWTH Aachen, 2017, http://dx.doi.org/10.18154/RWTH-2017-09944.
[11] A.K. Padhi, Phospho-olivines as positive-electrode materials for rechargeable lithium batteries, J. Electrochem. Soc. 144 (4) (1997) 1188, http://dx.doi.org/10.1149/1.1837571.
[12] V. Viswanathan, L.N. Palaniswamy, P.B. Leelavinodhan, Optimization techniques of battery packs using re-configurability: A review, J. Energy Storage 23 (2019) 404–415, http://dx.doi.org/10.1016/j.est.2019.03.002.
[13] K. Jacqué, L. Koltermann, J. Figgener, S. Zurmühlen, D.U. Sauer, The influence of frequency containment reserve on the operational data and the state of health of the hybrid stationary large-scale storage system, Energies 15 (4) (2022) 1342, http://dx.doi.org/10.3390/en15041342.
[14] J. Chen, Y. Zhang, W. Li, W. Cheng, Q. Zhu, State of charge estimation for lithium-ion batteries using gated recurrent unit recurrent neural network and adaptive Kalman filter, J. Energy Storage 55 (2022) 105396, http://dx.doi.org/10.1016/j.est.2022.105396.

[15] C. Hu, L. Ma, S. Guo, G. Guo, Z. Han, Deep learning enabled state-of-charge estimation of LiFePO4 batteries: A systematic validation on state-of-the-art charging protocols, Energy 246 (2022) 123404, http://dx.doi.org/10.1016/j.energy.2022.123404.
[16] T. Bank, S. Klamor, D.U. Sauer, Lithium-ion cell requirements in a real-world 48 V system and implications for an extensive aging analysis, J. Energy Storage 30 (2020) 101465, http://dx.doi.org/10.1016/j.est.2020.101465.
[17] K. Jacqué, L. Koltermann, J. Figgener, S. Zurmühlen, D.U. Sauer, The influence of frequency containment reserve on the cycles of a hybrid stationary large-scale storage system, J. Energy Storage 52 (2022) 105040, http://dx.doi.org/10.1016/j.est.2022.105040.
[18] E. Choi, S. Chang, A temperature-dependent state of charge estimation method including hysteresis for lithium-ion batteries in hybrid electric vehicles, IEEE Access 8 (2020) 129857–129868, http://dx.doi.org/10.1109/access.2020.3009281.
[19] G. Monsalve, A. Cardenas, D. Acevedo-Bueno, W. Martinez, Assessing the limits of equivalent circuit models and Kalman filters for estimating the state of charge: Case of agricultural robots, Energies 16 (7) (2023) 3133, http://dx.doi.org/10.3390/en16073133.
[20] H. Feng, Z. Wang, F. Zhang, H–adaptive H algorithm-based state of charge estimation considering the hysteresis effect for lithium polymer battery, Front. Energy Res. 9 (2021) http://dx.doi.org/10.3389/fenrg.2021.717722.
[21] Q. Liu, S. Liu, H. Liu, H. Qi, C. Ma, L. Zhao, Evaluation of LFP battery SoC estimation using auxiliary particle filter, Energies 12 (11) (2019) http://dx.doi.org/10.3390/en12112041.
[22] V.-H. Duong, H.A. Bastawrous, K. Lim, K.W. See, P. Zhang, S.X. Dou, Online state of charge and model parameters estimation of the LiFePO4 battery in electric vehicles using multiple adaptive forgetting factors recursive least-squares, J. Power Sources 296 (2015) 215–224, http://dx.doi.org/10.1016/j.jpowsour.2015.07.041.
[23] C. Zhang, K. Li, L. Pei, C. Zhu, An integrated approach for real-time model-based state-of-charge estimation of lithium-ion batteries, J. Power Sources 283 (2015) 24–36, http://dx.doi.org/10.1016/j.jpowsour.2015.02.099.
[24] J. Zhang, Y. Wei, H. Qi, State of charge estimation of LiFePO4 batteries based on online parameter identification, Appl. Math. Model. 40 (11) (2016) 6040–6050, http://dx.doi.org/10.1016/j.apm.2016.01.047.
[25] E. Ipek, M.K. Eren, M. Yilmaz, State-of-charge estimation of Li-ion battery cell using support vector regression and gradient boosting techniques, in: 2019 International Aegean Conference on Electrical Machines and Power Electronics, ACEMP, IEEE, 2019, http://dx.doi.org/10.1109/acemp-optim44294.2019.9007188.
[26] J. Chen, Y. Zhang, J. Wu, W. Cheng, Q. Zhu, SOC estimation for lithium-ion battery using the LSTM-RNN with extended input and constrained output, Energy 262 (2023) 125375, http://dx.doi.org/10.1016/j.energy.2022.125375.
[27] M. Kwak, B. Lkhagvasuren, J. Park, J.-H. You, Parameter identification and SOC estimation of a battery under the hysteresis effect, IEEE Trans. Ind. Electron. 67 (11) (2020) 9758–9767, http://dx.doi.org/10.1109/tie.2019.2956394.
[28] Y. Ma, J. Zhu, X. Li, Z. Tang, State of charge and state of health estimation based on dual nonlinear adaptive observer and hysteresis model of lithium-ion battery, J. Renew. Sustain. Energy 13 (4) (2021) http://dx.doi.org/10.1063/5.0058265.
[29] M. Chen, F. Han, L. Shi, Y. Feng, C. Xue, W. Gao, J. Xu, Sliding mode observer for state-of-charge estimation using hysteresis-based Li-ion battery model, Energies 15 (7) (2022) 2658, http://dx.doi.org/10.3390/en15072658.
[30] Y. Ko, W. Choi, A new SOC estimation for LFP batteries: Application in a 10 ah cell (HW 38120 L/S) as a hysteresis case study, Electronics 10 (6) (2021) 705, http://dx.doi.org/10.3390/electronics10060705.
[31] Z. Xu, J. Wang, Q. Fan, P.D. Lund, J. Hong, Improving the state of charge estimation of reused lithium-ion batteries by abating hysteresis using machine learning technique, J. Energy Storage 32 (2020) 101678, http://dx.doi.org/10.1016/j.est.2020.101678.
[32] H. Movahedi, N. Tian, H. Fang, R. Rajamani, Hysteresis compensation and nonlinear observer design for state-of-charge estimation using a nonlinear double-capacitor Li-ion battery model, IEEE/ASME Trans. Mechatronics 27 (1) (2022) 594–604, http://dx.doi.org/10.1109/tmech.2021.3068982.
[33] M. Xu, E. Zhang, S. Wang, Y. Shen, B. Zou, H. Li, Y. Wan, K. Wang, K. Jiang, Dynamic ultrasonic response modeling and accurate state of charge estimation for lithium ion batteries under various load profiles and temperatures, Appl. Energy 355 (2024) 122210, http://dx.doi.org/10.1016/j.apenergy.2023.122210.
[34] S. Huang, J. Kang, B. Zhao, O. Wu, J.V. Wang, A SOC correction method based on unsynchronized full charge and discharge control strategy in multi-branch battery system, Energies 16 (17) (2023) 6287, http://dx.doi.org/10.3390/en16176287.
[35] K.V.V.K. Chaitanya, M. Bayya, State estimation algorithms for electric vehicle 48 V battery management system, Mater. Today: Proc. 72 (2023) 199–203, http://dx.doi.org/10.1016/j.matpr.2022.07.044.
[36] G. Zhu, O. Wu, Q. Wang, J. Kang, J.V. Wang, The modeling and SOC estimation of a LiFePO4 battery considering the relaxation and overshoot of polarization voltage, Batteries 9 (7) (2023) 369, http://dx.doi.org/10.3390/batteries9070369.
[37] S. Mao, X. Han, Y. Lu, D. Wang, A. Su, L. Lu, X. Feng, M. Ouyang, Multi sensor fusion methods for state of charge estimation of smart lithium-ion batteries, J. Energy Storage 72 (2023) 108736, http://dx.doi.org/10.1016/j.est.2023.108736.
[38] J. Hou, J. Xu, C. Lin, D. Jiang, X. Mei, State of charge estimation for lithium-ion batteries based on battery model and data-driven fusion method, Energy 290 (2024) 130056, http://dx.doi.org/10.1016/j.energy.2023.130056.
[39] M. Liu, J. Xu, Y. Jiang, X. Mei, Multi-dimensional features based data-driven state of charge estimation method for LiFePO4 batteries, Energy 274 (2023) 127407, http://dx.doi.org/10.1016/j.energy.2023.127407.
[40] S. Mao, M. Han, X. Han, L. Lu, X. Feng, A. Su, D. Wang, Z. Chen, Y. Lu, M. Ouyang, An electrical–thermal coupling model with artificial intelligence for state of charge and residual available energy co-estimation of LiFePO4 battery system under various temperatures, Batteries 8 (10) (2022) 140, http://dx.doi.org/10.3390/batteries8100140.
[41] A. Marongiu, F.G.W. Nußbaum, W. Waag, M. Garmendia, D.U. Sauer, Comprehensive study of the influence of aging on the hysteresis behavior of a lithium iron phosphate cathode-based lithium ion battery - an experimental investigation of the hysteresis, Appl. Energy 171 (2016) 629–645, http://dx.doi.org/10.1016/j.apenergy.2016.02.086.
[42] D. Li, H. Zhou, Two-phase transition of Li-intercalation compounds in Li-ion batteries, Mater. Today 17 (9) (2014) 451–463, http://dx.doi.org/10.1016/j.mattod.2014.06.002.
[43] W. Waag, Adaptive Algorithms for Monitoring of Lithium-Ion Batteries in Electric Vehicles (Dissertation), RWTH Aachen, Aachen, 2014, URL https://publications.rwth-aachen.de/record/444480.
[44] R. Xiong, J. Cao, Q. Yu, H. He, F. Sun, Critical review on the battery state of charge estimation methods for electric vehicles, IEEE Access 6 (2018) 1832–1843, http://dx.doi.org/10.1109/access.2017.2780258.
[45] S. Pang, J. Farrell, J. Du, M. Barth, Battery state-of-charge estimation, in: Proceedings of the 2001 American Control Conference. (Cat. No.01CH37148), Vol. 2, IEEE, 2001, pp. 1644–1649, http://dx.doi.org/10.1109/acc.2001.945964.
[46] A. Berrueta, I.S. Martin, P. Sanchis, A. Ursua, Comparison of state-of-charge estimation methods for stationary lithium-ion batteries, in: IECON 2016 - 42nd Annual Conference of the IEEE Industrial Electronics Society, IEEE, 2016, pp. 2010–2015, http://dx.doi.org/10.1109/iecon.2016.7794094.
[47] X. Hu, F. Sun, Y. Zou, Estimation of state of charge of a lithium-ion battery pack for electric vehicles using an adaptive luenberger observer, Energies 3 (9) (2010) 1586–1603, http://dx.doi.org/10.3390/en3091586.
[48] J. Li, J.K. Barillas, C. Guenther, M.A. Danzer, A comparative study of state of charge estimation algorithms for LiFePO4 batteries used in electric vehicles, J. Power Sources 230 (2013) 244–250, http://dx.doi.org/10.1016/j.jpowsour.2012.12.057.
[49] E. Wan, R.V.D. Merwe, The unscented Kalman filter for nonlinear estimation, in: Proceedings of the IEEE 2000 Adaptive Systems for Signal Processing, Communications, and Control Symposium (Cat. No.00EX373), IEEE, 2002, pp. 153–158, http://dx.doi.org/10.1109/asspcc.2000.882463.
[50] G.L. Plett, Sigma-point Kalman filtering for battery management systems of LiPB-based HEV battery packs part 1: Introduction and state estimation, J. Power Sources 161 (2) (2006) 1356–1368, http://dx.doi.org/10.1016/j.jpowsour.2006.06.003.
[51] G.L. Plett, Sigma-point Kalman filtering for battery management systems of LiPB-based HEV battery packs part 2: Simultaneous state and parameter estimation, J. Power Sources 161 (2) (2006) 1369–1384, http://dx.doi.org/10.1016/j.jpowsour.2006.06.004.
[52] J. Kim, G.-S. Seo, C. Chun, B.-H. Cho, S. Lee, OCV hysteresis effect-based SOC estimation in extended Kalman filter algorithm for a LiFePO4/C cell, in: 2012 IEEE International Electric Vehicle Conference, IEEE, 2012, pp. 1–5, http://dx.doi.org/10.1109/ievc.2012.6183174.
[53] A. Sidhu, A. Izadian, S. Anwar, Adaptive nonlinear model-based fault diagnosis of Li-ion batteries, IEEE Trans. Ind. Electron. 62 (2) (2015) 1002–1011, http://dx.doi.org/10.1109/tie.2014.2336599.
[54] H. He, R. Xiong, X. Zhang, F. Sun, J. Fan, State-of-charge estimation of the lithium-ion battery using an adaptive extended Kalman filter based on an improved thevenin model, IEEE Trans. Veh. Technol. 60 (4) (2011) 1461–1469, http://dx.doi.org/10.1109/tvt.2011.2132812.
[55] D. Andre, C. Appel, T. Soczka-Guth, D.U. Sauer, Advanced mathematical methods of SOC and SOH estimation for lithium-ion batteries, J. Power Sources 224 (2013) 20–27, http://dx.doi.org/10.1016/j.jpowsour.2012.10.001.
[56] F. Ringbeck, M. Garbade, D.U. Sauer, Uncertainty-aware state estimation for electrochemical model-based fast charging control of lithium-ion batteries, J. Power Sources 470 (2020) 228221, http://dx.doi.org/10.1016/j.jpowsour.2020.228221.
[57] W. Li, Y. Fan, F. Ringbeck, D. Jöst, X. Han, M. Ouyang, D.U. Sauer, Electrochemical model-based state estimation for lithium-ion batteries with adaptive unscented Kalman filter, J. Power Sources 476 (2020) 228534, http://dx.doi.org/10.1016/j.jpowsour.2020.228534.
[58] D. Jiani, W. Youyi, W. Changyun, Li-ion battery SOC estimation using particle filter based on an equivalent circuit model, in: 2013 10th IEEE International Conference on Control and Automation, ICCA, IEEE, 2013, pp. 580–585, http://dx.doi.org/10.1109/icca.2013.6565047.

[59] S. Schwunk, N. Armbruster, S. Straub, J. Kehl, M. Vetter, Particle filter for state of charge and state of health estimation for lithium–iron phosphate batteries, J. Power Sources 239 (2013) 705–710, http://dx.doi.org/10.1016/j.jpowsour.2012.10.058.

[60] W. Yan, G. Niu, S. Tang, B. Zhang, State-of-charge estimation of lithium-ion batteries by lebesgue sampling-based EKF method, in: IECON 2017 - 43rd Annual Conference of the IEEE Industrial Electronics Society, IEEE, 2017, http://dx.doi.org/10.1109/iecon.2017.8216546.

[61] R. Xiong, X. Gong, C.C. Mi, F. Sun, A robust state-of-charge estimator for multiple types of lithium-ion batteries using adaptive extended Kalman filter, J. Power Sources 243 (2013) 805–816, http://dx.doi.org/10.1016/j.jpowsour.2013.06.076.

[62] T. Bengtsson, P. Bickel, B. Li, Curse-of-dimensionality revisited: Collapse of the particle filter in very large scale systems, in: Institute of Mathematical Statistics Collections, Institute of Mathematical Statistics, 2008, pp. 316–334, http://dx.doi.org/10.1214/193940307000000518.

[63] N. Ikoma, N. Ichimura, T. Higuchi, H. Maeda, Maneuvering target tracking by using particle filter, in: Proceedings Joint 9th IFSA World Congress and 20th NAFIPS International Conference (Cat. No. 01TH8569), IEEE, 2001, http://dx.doi.org/10.1109/nafips.2001.944415.

[64] S. Thrun, W. Burgard, D. Fox, Probabilistic Robotics, The MIT Press, 2005, URL https://www.ebook.de/de/product/3701211/sebastian_thrun_wolfram_burgard_dieter_fox_probabilistic_robotics.html.

[65] L. Koltermann, M. Celi Cortés, J. Figgener, S. Zurmühlen, D.U. Sauer, Power curves of megawatt-scale battery storage technologies for frequency regulation and energy trading, Appl. Energy 347 (2023) 121428, http://dx.doi.org/10.1016/j.apenergy.2023.121428.

[66] RWTH Aachen University, ISEA, Modular multi-megawatt multi-technology medium voltage battery storage system, 2024, https://m5bat.isea.rwth-aachen.de/. (Visited 02 April 2024).

[67] D. Jöst, L.N. Palaniswamy, K.L. Quade, D.U. Sauer, Dataset for towards robust state estimation for LFP batteries: Model-in-the-loop analysis with hysteresis modeling and perspectives for other chemistries, 2024, http://dx.doi.org/10.18154/RWTH-2024-03667, Dataset.

[68] D. Jöst, H. Zappen, D.U. Sauer, Methodology for model-based battery management algorithm validation, benchmarking and application-oriented selection, in: ICAE 2019 - 11th International Conference on Applied Energy, 2019, http://dx.doi.org/10.13140/RG.2.2.32086.80964.

[69] F.E. Hust, Physico-Chemically Motivated Parameterization and Modelling of Real-Time Capable Lithium-Ion Battery Models: A Case Study on the Tesla Model S Battery (Dissertation), RWTH Aachen ISEA, Aachen, 2018, http://dx.doi.org/10.18154/RWTH-2019-00249.

[70] J.K. Barillas, J. Li, C. Günther, M.A. Danzer, A comparative study and validation of state estimation algorithms for Li-ion batteries in battery management systems, Appl. Energy 155 (2015) 455–462, http://dx.doi.org/10.1016/j.apenergy.2015.05.102.

[71] S. Zhao, S.R. Duncan, D.A. Howey, Observability analysis and state estimation of lithium-ion batteries in the presence of sensor biases, IEEE Trans. Control Syst. Technol. 25 (1) (2017) 326–333, http://dx.doi.org/10.1109/tcst.2016.2542115.

[72] X. Lin, Theoretical analysis of battery SOC estimation errors under sensor bias and variance, IEEE Trans. Ind. Electron. 65 (9) (2018) 7138–7148, http://dx.doi.org/10.1109/tie.2018.2795521.

[73] A. Barai, W.D. Widanage, J. Marco, A. McGordon, P. Jennings, A study of the open circuit voltage characterization technique and hysteresis assessment of lithium-ion cells, J. Power Sources 295 (2015) 99–107, http://dx.doi.org/10.1016/j.jpowsour.2015.06.140.

[74] M. Lelie, T. Braun, M. Knips, H. Nordmann, F. Ringbeck, H. Zappen, D.U. Sauer, Battery management system hardware concepts: An overview, Appl. Sci. 8 (4) (2018) 534, http://dx.doi.org/10.3390/app8040534.

[75] T. Nemeth, P. Schröer, M. Kuipers, D.U. Sauer, Lithium titanate oxide battery cells for high-power automotive applications – electro-thermal properties, aging behavior and cost considerations, J. Energy Storage 31 (2020) 101656, http://dx.doi.org/10.1016/j.est.2020.101656.

[76] X. Han, M. Ouyang, L. Lu, J. Li, Cycle life of commercial lithium-ion batteries with lithium titanium oxide anodes in electric vehicles, Energies 7 (8) (2014) 4895–4909, http://dx.doi.org/10.3390/en7084895.

[77] L. Wang, Z. Wang, Q. Ju, W. Wang, Z. Wang, Characteristic analysis of lithium titanate battery, Energy Procedia 105 (2017) 4444–4449, http://dx.doi.org/10.1016/j.egypro.2017.03.942.

[78] G. Patry, A. Romagny, S. Martinet, D. Froelich, Cost modeling of lithium-ion battery cells for automotive applications, Energy Sci. Eng. 3 (1) (2014) 71–82, http://dx.doi.org/10.1002/ese3.47.

[79] J. Dölle, Investigation of Si/C Based Anodes for Li-Ion Batteries (Dissertation), TU Berlin, 2014, http://dx.doi.org/10.14279/DEPOSITONCE-4229.

[80] C. Jin, H. Li, Y. Song, B. Lu, A.K. Soh, J. Zhang, On stress-induced voltage hysteresis in lithium ion batteries: Impacts of surface effects and interparticle compression, Sci. China Technol. Sci. 62 (8) (2019) 1357–1364, http://dx.doi.org/10.1007/s11431-018-9491-6.

[81] B. Lu, Y. Song, Q. Zhang, J. Pan, Y.-T. Cheng, J. Zhang, Voltage hysteresis of lithium ion batteries caused by mechanical stress, Phys. Chem. Chem. Phys. 18 (6) (2016) 4721–4727, http://dx.doi.org/10.1039/c5cp06179b.

[82] A. Marongiu, N. Nlandi, Y. Rong, D.U. Sauer, On-board capacity estimation of lithium iron phosphate batteries by means of half-cell curves, J. Power Sources 324 (2016) 158–169, http://dx.doi.org/10.1016/j.jpowsour.2016.05.041.